



Enhanced photocatalytic oxidation of NO over g-C₃N₄-TiO₂ under UV and visible light



Jinzhu Ma, Caixia Wang, Hong He*

State Key Joint Laboratory of Environment Simulation and Pollution Control, Research Center for Eco-Environmental Sciences, Chinese Academy of Sciences, Beijing 100085, China

ARTICLE INFO

Article history:

Received 22 September 2015

Received in revised form

12 November 2015

Accepted 14 November 2015

Available online 19 November 2015

Keywords:

TiO₂

Graphitic-C₃N₄

Photocatalysis

NO_x removal

Radical species

ABSTRACT

In this work, graphitic carbon nitride-titanium dioxide (g-C₃N₄-TiO₂) was successfully prepared by a facile calcination route utilizing commercial P25 and melamine as the precursors. The as-prepared g-C₃N₄/TiO₂ photocatalysts were characterized systematically to elucidate their morphological structure and physico-chemical properties. The photocatalytic performance of g-C₃N₄-TiO₂ composites was investigated for the removal of NO_x in air. At the optimal g-C₃N₄ content (~15 wt%, labeled as M400), the conversion of NO_x was 27%, which is higher than that of pure P25 (17%) and g-C₃N₄ (7%) under visible light. The activity of M400 was also enhanced under UV light. However, a mechanically mixed g-C₃N₄ and TiO₂ sample (with the content of g-C₃N₄ the same as M400, labeled as M0 + g-C₃N₄) did not improve the conversion of NO_x. Therefore, the interaction of g-C₃N₄ and P25 is important for the activity. EPR results indicated that •O₂⁻ is the main active species for NO oxidation to NO₃⁻ under visible and UV light, which is responsible for the difference in activity between M400 and M0 + g-C₃N₄. The present study can improve our understanding of NO removal on the photocatalyst surface and the mechanism for the activity enhancement by the formation of g-C₃N₄-TiO₂.

© 2015 The Authors. Published by Elsevier B.V. This is an open access article under the CC BY-NC-ND license (<http://creativecommons.org/licenses/by-nc-nd/4.0/>).

1. Introduction

Nitrogen oxides (NO_x), mainly derived from the combustion of fossil fuels, are responsible for environmental problems such as acid rain, photochemical smog, haze, and so on [1,2]. Over the past decades, the concentration of NO_x in the atmosphere has greatly increased because of the fast growth of energy consumption [1]. Selective catalytic reduction (SCR), wet scrubbing, adsorption, biofiltration, and catalytic decomposition, can remove NO_x from emission sources; however, they cannot be used for the removal of NO_x at parts per billion (ppb) levels in the air [3,4]. Semiconductor photocatalysis, as a “green” technology that utilizes sunlight to decompose air pollutants at ambient conditions, has been used to remove low concentration NO_x [5–11].

Recently, graphitic carbon nitride (g-C₃N₄) has turned out to be a fascinating choice for a photocatalyst due to its high stability with respect to thermal (up to 600 °C in air) and chemical attacks (e.g., acid, base, and organic solvents) and an appealing electronic structure, having a medium band gap [12–14]. Graphitic-C₃N₄ has

been used for the photocatalytic removal of NO in air [10,15–17]. Because of its small surface area and fast electron-hole recombination, the application of g-C₃N₄ is not ideal [18]. Mesoporous g-C₃N₄ with specific surface area of 200–500 m²/g can provide more sites for the reaction; however, a template is often needed in the preparation, which is complicated [19–22]. A composite of g-C₃N₄ and metal oxide can improve the surface area of the photocatalyst and promote the separation of photogenerated electrons and holes, so as to improve the photocatalytic activity. Compared with the traditional TiO₂ photocatalyst, the conduction band electrons of g-C₃N₄ have stronger reduction ability, and can effectively activate molecular oxygen and produce more superoxide radicals for photocatalytic degradation of pollutants [12]. g-C₃N₄-TiO₂ composites have been widely investigated for the photocatalytic degradation of pollutants, and g-C₃N₄ modification was found to effectively enhance the activity of photocatalysts [23–35]. In all these studies, TiO₂ was prepared during the experimental processes, but there were a few reports about composites prepared with P25, the well-known popular commercial photocatalyst with the best photocatalytic activity under UV irradiation [36–38]. Importantly, the studies mostly investigated the effect on the visible light activity [36,38] and ignored the effect on the UV light activity, which is also important for the practical application of photocatalysts in the

* Corresponding author. Fax: +86 10 62849123.
E-mail address: honghe@rcees.ac.cn (H. He).

outdoors. Additionally, to the best of our knowledge, the use of g-C₃N₄-TiO₂ materials for photocatalytic removal of NO_x has not been reported.

In this work, g-C₃N₄-TiO₂ was successfully prepared by a facile calcination route utilizing commercial P25 and melamine as the precursors. The as-prepared g-C₃N₄/TiO₂ photocatalysts were characterized by XRD, TGA, Raman, TEM, XPS, N₂ adsorption–desorption, UV–vis, PL and EPR. The photocatalytic performance was systematically evaluated for removal of NO_x under visible and UV light.

2. Experimental

2.1. Catalyst synthesis

The photocatalysts were synthesized by calcining mixtures of P25 and melamine. In a typical synthesis procedure, 1 g P25 was dispersed in 30 mL distilled water, and then a given amount of melamine was added. The mixed solution was uniformly agitated for 30 min, and then dried in air at 60 °C. Finally, the mixture was sealed in a crucible with a cover, which was then maintained at 550 °C in a muffle furnace (the heating ramp is 15 °C/min) for 4 h and the atmosphere for the heating process is air. The weight percentage ratio of melamine against P25 in the precursors was controlled to be 0, 65, 300, 330, 400, 500 and 600 wt%, and the resulting photocatalysts were labeled as M0 (P25), M65, M300, M330, M400, M500 and M600, respectively. The actual loading amounts of g-C₃N₄ on the M65, M300, M330, M400, M500 and M600 samples were estimated to be about 0.1, 0.58, 3.23, 15.06, 36.75 and 55.93 wt%, respectively (determined by TGA, See Fig. S1). Pure g-C₃N₄ was prepared (with the absence of P25) for comparison. A photocatalyst having the same content of g-C₃N₄ as M400 was prepared by mechanical mixing of the appropriate amount of M0 and pure g-C₃N₄, and labeled as M0 + g-C₃N₄. The amount of g-C₃N₄ in M0 + g-C₃N₄ was determined to be 15.62 wt% by TGA (data not shown).

2.2. Characterization

The crystalline structure of the samples were determined by a powder X-ray diffractometer (XRD; X'Pert PRO, PANalytical, Netherlands) using Cu K α (λ = 0.15406 nm) radiation. The data of 2 θ from 20° to 80° were collected with the step size of 0.05°.

The contents of g-C₃N₄ of the as-prepared photocatalysts were characterized using thermal gravimetric analysis (TGA) with a TGA/DSC1 STAR^c system (METTLER TOLEDO). About 15 mg of each photocatalyst was heated up to 800 °C under 100 mL/min air flow at a heating rate of 10 °C/min.

Raman spectra of the photocatalysts were recorded on a home-made UV resonance Raman spectrometer (UVR DLPC-DL-03), which was calibrated against the Stokes Raman signal of Teflon at 1378 cm⁻¹. A 532 nm laser beam and a 325 nm He–Cd laser was used as an exciting source for the measurement of Raman.

Transmission electron microscopy (TEM) images were obtained using a JEOL JEM-2100 electron microscope (JEOL, Japan).

X-ray photoelectron spectroscopy (XPS) of the samples were recorded on a Scanning X-ray Microprobe (AXIS Ultra, Kratos Analytical, Inc.) using Al K α radiation. Binding energies were calibrated using the C 1s peak (BE = 284.8 eV) as standard.

The specific surface area of the photocatalysts were determined with a physisorption analyzer (Autosorb-1C-TCD, Quantachrome, USA) by N₂ adsorption–desorption at 77 K. Prior to the N₂ physisorption, all samples were degassed at 300 °C for 5 h.

The UV–vis diffuse reflection spectra were recorded in air with BaSO₄ as a reference with a diffuse reflectance UV–vis Spectrophotometer (U-3310, Hitachi).

The photoluminescence (PL) spectra of the photocatalysts were measured in a home-built laser-induced luminescence spectrograph. Prior to the experiments, the wavelength was calibrated with a mercury lamp. A 325 nm He–Cd laser was used as the exciting source.

The X-band electron paramagnetic resonance (EPR) spectra were recorded at room temperature using a Bruker A300-10/12 EPR spectrometer. The sample for EPR measurement was prepared by adding the photocatalysts to a 0.08 mol/L 5,5'-dimethyl-1-pyrroline-*N*-oxide (DMPO) solution with aqueous dispersion for DMPO- \cdot OH and methanol dispersion for DMPO- \cdot O₂⁻. The photocatalysts was irradiated with the aforementioned visible light or UV light for 5 min. The EPR measurement was performed immediately after the illumination. Typical instrumental settings were as follows: microwave power 23.16 mW, microwave frequency 9.85 GHz, modulation frequency 100 kHz, modulation amplitude 3 G, time-constant 20.48 ms, sweep time 81.92 s.

2.3. Photocatalytic NO removal

The photocatalytic experiments for the removal of NO with the resulting samples were performed at ambient temperature in a continuous flow reactor, similar to our previous work [39,40] and are fully described in SI. Briefly, for the visible light photocatalytic activity test, a 500-W commercial Xenon arc lamp (Beijing TrusTech Science and Technology Co., China) with two optical filters were used to obtain light in the 420–700 nm range, and the integrated light intensity was 35.8 mW/cm². For the UV light photocatalytic activity test, a 500-W commercial Hg lamp (Beijing TrusTech Science and Technology Co., China) was used as the light source with an optical filter (λ = 365–366 nm), and the average light intensity was 84.7 mW/cm². 0.05 g photocatalysts was used for each experiment. The initial concentration of NO was 400 ppb and the relatively humidity of the gas was 55%. The total flow rate was controlled at 1.2 L min⁻¹. The concentration of NO, NO₂ and NO_x was measured by a chemiluminescence NO_x analyzer (Thermo Environmental Instruments Inc. Model 42i).

The NO conversion, NO₂ selectivity and NO_x conversion were defined as follows:

$$\text{NO conversion} = \frac{[\text{NO}]_{\text{in}} - [\text{NO}]_{\text{out}}}{[\text{NO}]_{\text{in}}}$$

$$\text{NO}_2 \text{ selectivity} = \frac{[\text{NO}_2]_{\text{out}}}{[\text{NO}]_{\text{in}} - [\text{NO}]_{\text{out}}}$$

$$\text{NO}_x \text{ conversion} = \frac{[\text{NO}]_{\text{in}} - [\text{NO}_x]_{\text{out}}}{[\text{NO}]_{\text{in}}}$$

3. Results and discussion

3.1. Photocatalytic NO removal activity

NO cannot be removed with or without light in the absence of photocatalyst (residence time 5.7 s). The NO conversion, NO_x conversion and NO₂ selectivity at 0.5 h for various photocatalysts under visible light are displayed in Fig. S2. It can be seen that the incorporation of g-C₃N₄ on P25 can improve the conversion of NO_x. The photocatalytic activity of the g-C₃N₄/P25 photocatalyst is highly dependent on the amount of g-C₃N₄. The conversion of NO_x on M400 was higher than that of other photocatalysts; this means that the optimum g-C₃N₄ content is ~15 wt%. Therefore, we chose M400

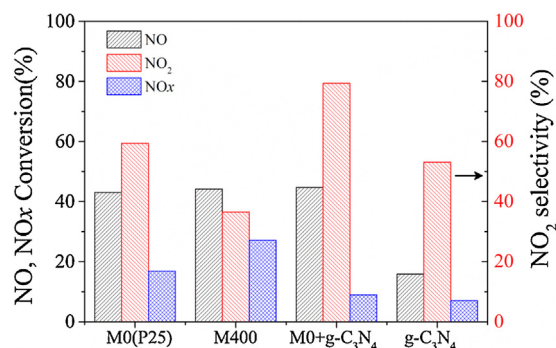


Fig. 1. The NO conversion, NO_x conversion and NO₂ selectivity at 0.5 h for M0, M400, M0 + g-C₃N₄ and g-C₃N₄ under visible light.

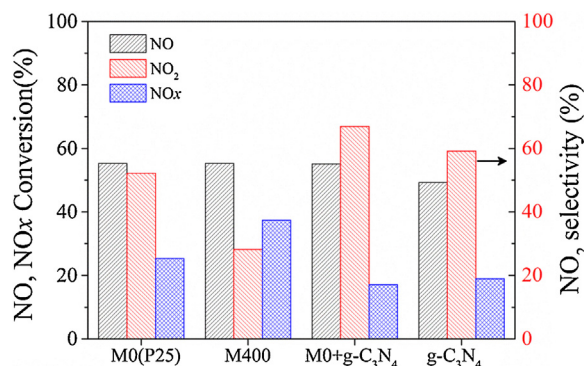


Fig. 2. The NO conversion, NO_x conversion and NO₂ selectivity at 0.5 h for M0, M400, M0 + g-C₃N₄ and g-C₃N₄ under UV light.

as the optimal content to carry out our further investigations. Fig. 1 shows the NO conversion, NO_x conversion and NO₂ selectivity at 0.5 h for M0, M400, M0 + g-C₃N₄ and g-C₃N₄ under visible light. As we can see, the conversion of NO was about 44% over M0, M400 and M0 + g-C₃N₄, however, the NO₂ selectivity (~36%) was lowest over M400, and therefore the conversion of NO_x (~27%) was highest over M400. The activity of M400 was higher than that the sum of M0 (17%) and g-C₃N₄ (7%). However, the photocatalysts prepared by mechanical mixing of g-C₃N₄ (the same content with M400) and M0 did not improve the conversion of NO_x (The conversion of NO was similar to that of M400, but the NO₂ selectivity for (~80%) was high.). Therefore, the interaction of g-C₃N₄ and P25 is important for the activity, which will be discussed in the following part.

Because of P25 is a well-known UV-response photocatalyst, the activity under UV light is also important for the practical application of the photocatalysts. Fig. 2 shows the NO conversion, NO_x conversion and NO₂ selectivity at 0.5 h for M0, M400, M0 + g-C₃N₄ and g-C₃N₄ under UV light. Similar to the visible light activity, the UV light activity of M400 was enhanced, but the photocatalyst prepared by mechanical mixing of g-C₃N₄ (the same content as M400) and M0 did not improve the conversion of NO_x. These results further indicate that the interaction of g-C₃N₄ and P25 is important for the activity.

3.2. The crystal structure of the photocatalysts

XRD was used to determine the phase structures and average crystal size of the as-prepared photocatalysts. Fig. 3 illustrates the XRD patterns of photocatalysts prepared at different weight ratios of g-C₃N₄ and TiO₂. It can be seen that the TiO₂ phases in pure P25 (M0) and the g-C₃N₄/P25 photocatalysts (M65, M175, M400, M500, M600 and M0 + g-C₃N₄) were anatase (JCPDS no. 21–1272) and rutile (JCPDS no. 21–1276), and the weight ratio of anatase was

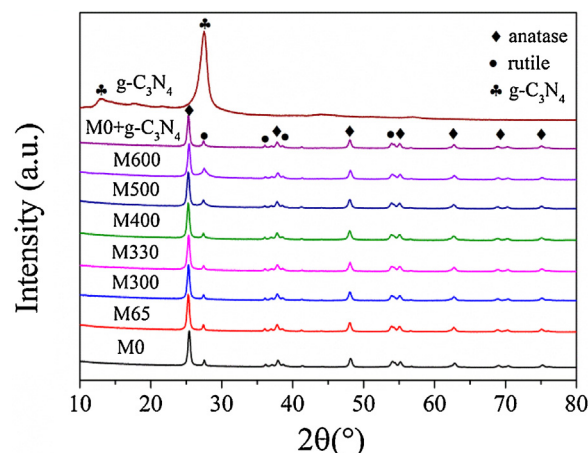


Fig. 3. XRD patterns of M0, M65, M300, M330, M400, M500, M600, M0 + g-C₃N₄ and pure g-C₃N₄.

about 80%. For pure g-C₃N₄, two main diffraction peaks at $2\theta = 27.5^\circ$ and 13.0° can be observed, which indicates the formation of g-C₃N₄ (JCPDS no. 87–1526). The stronger peak at 27.4° was the (002) diffraction peak and represents the interplanar graphitic stacking with an interlayer distance of 0.325 nm. The minor peak at around 13.0° corresponds to the (100) diffraction peak and represents an interplanar separation of 0.681 nm [10,41]. No obvious changes of the positions and intensities of the characteristic diffraction peaks of anatase and rutile were observed for any of the g-C₃N₄/P25 photocatalysts. This implies that the existence of g-C₃N₄ did not have a significant influence on the phase structure of TiO₂ in the as-prepared photocatalysts. The crystallite size of the photocatalyst was determined from the half-width of peaks by using Scherrer's formula ($d = 0.9\lambda / \beta \cos \theta$) on the basis of the anatase [101] and rutile [110] peaks. All g-C₃N₄/P25 photocatalysts have almost the same crystallite size (ca. 21 nm for anatase and 33 nm for rutile), indicating that the addition of g-C₃N₄ has no obvious influence on the crystallite size and morphology of TiO₂.

3.3. The interaction between g-C₃N₄ and TiO₂

Raman spectroscopy can be used to clearly characterize the surface structure of photocatalysts. Visible Raman spectra of M0, M400, M0 + g-C₃N₄ and g-C₃N₄ are displayed in Fig. S3. The presence of g-C₃N₄ results in a strong fluorescence on TiO₂. From the fluorescence signal intensity, it can be seen the content of g-C₃N₄ on the surface of M400 is higher than that on the surface of M0 + g-C₃N₄. UV Raman spectroscopy was found to be more sensitive to the surface region of TiO₂ than visible Raman spectroscopy and XRD because TiO₂ strongly absorbs UV light [42]. Fig. 4 illustrates the UV Raman spectra of M0, M400, M0 + g-C₃N₄ and g-C₃N₄. For g-C₃N₄, several characteristic peaks at 1624, 1576, 1481, 1258, 976, 759, 704, 582 and 474 cm⁻¹ were observed, corresponding to the typical vibration modes of CN heterocycles [43,44]. The characteristic peaks of TiO₂ and weak characteristic peaks of g-C₃N₄ were observed on the surface of M400 and M0 + g-C₃N₄. The characteristic peaks of g-C₃N₄ were more pronounced on the surface of M400, which further reveals that the content of g-C₃N₄ on the surface of M400 is higher than that on the surface of M0 + g-C₃N₄. These results indicate that g-C₃N₄ is more evenly distributed on the surface of M400 than that on the surface of M0 + g-C₃N₄.

The morphology of the photocatalyst was examined by TEM. Fig. 5 shows the TEM micrographs of M0, M400, M0 + g-C₃N₄ and g-C₃N₄. It can be seen that pure TiO₂ (Fig. 5a) shows spherical particles whereas pure g-C₃N₄ (Fig. 5d) displays a 2D lamellar structure. For M400 (Fig. 5b), the TiO₂ nanoparticles are embedded in the g-C₃N₄

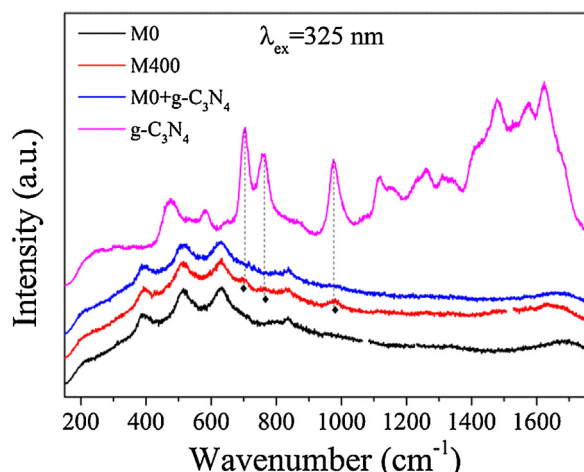


Fig. 4. UV Raman spectroscopy of M0, M400, M0 + g-C₃N₄ and g-C₃N₄.

lamellar structure. For the M0 + g-C₃N₄ sample (Fig. 5c), parts of the TiO₂ nanoparticles are embedded in the g-C₃N₄ lamellar structure. These observations were consistent with the Raman results, further indicating that g-C₃N₄ is more evenly distributed on the surface of M400 than on the surface of M0 + g-C₃N₄. These observations suggest the formation of a heterojunction between TiO₂ and g-C₃N₄, which would be an ideal system to achieve improved electron-hole separation [37].

More detailed information regarding the chemical composition of the as-prepared photocatalysts and the chemical status of the Ti, C and N elements in the photocatalyst was obtained using X-ray photoelectron spectroscopy. The survey spectrum of M0, M400, M0 + g-C₃N₄ and g-C₃N₄ is shown in Fig. S4. The g-C₃N₄ sample exhibited C1s and N1s signals with a C/N molar ratio of 0.75 (Table S1), in agreement with the ideal C₃N₄ composition (C/N = 0.75). As shown in Table S1, More N atoms and less O and Ti atoms were observed for M400 than that for M0 + g-C₃N₄, which indicates that g-C₃N₄ is more uniformly dispersed on the surface of M400, consistent with the Raman and TEM results.

The BET specific surface areas of the M0, M400, M0 + g-C₃N₄ and g-C₃N₄ samples were 41.9 m²/g, 60.8 m²/g, 53.4 m²/g and 18.0 m²/g, respectively. The increase of the BET specific surface areas of M400 may be due to that TiO₂ nanoparticles embedded in the g-C₃N₄ lamellar structure leads to the formation of thinner lamellar g-C₃N₄ for g-C₃N₄-TiO₂. For M0 + g-C₃N₄, the grinding may leads to the exfoliation of g-C₃N₄, which increases the BET surface areas of the photocatalysts. This needs to be studied further. However, this is not the focus of this study. The BET specific surface area of M400 and M0 + g-C₃N₄ was similar but the activity was different, indicating the surface area is not the key factor for the improvement of the activity.

3.4. UV-vis diffuse reflectance spectra and band structure

Fig. 6a shows the UV-vis diffuse reflectance spectra (DRS) of the synthesized photocatalysts. The band gap values of the synthe-

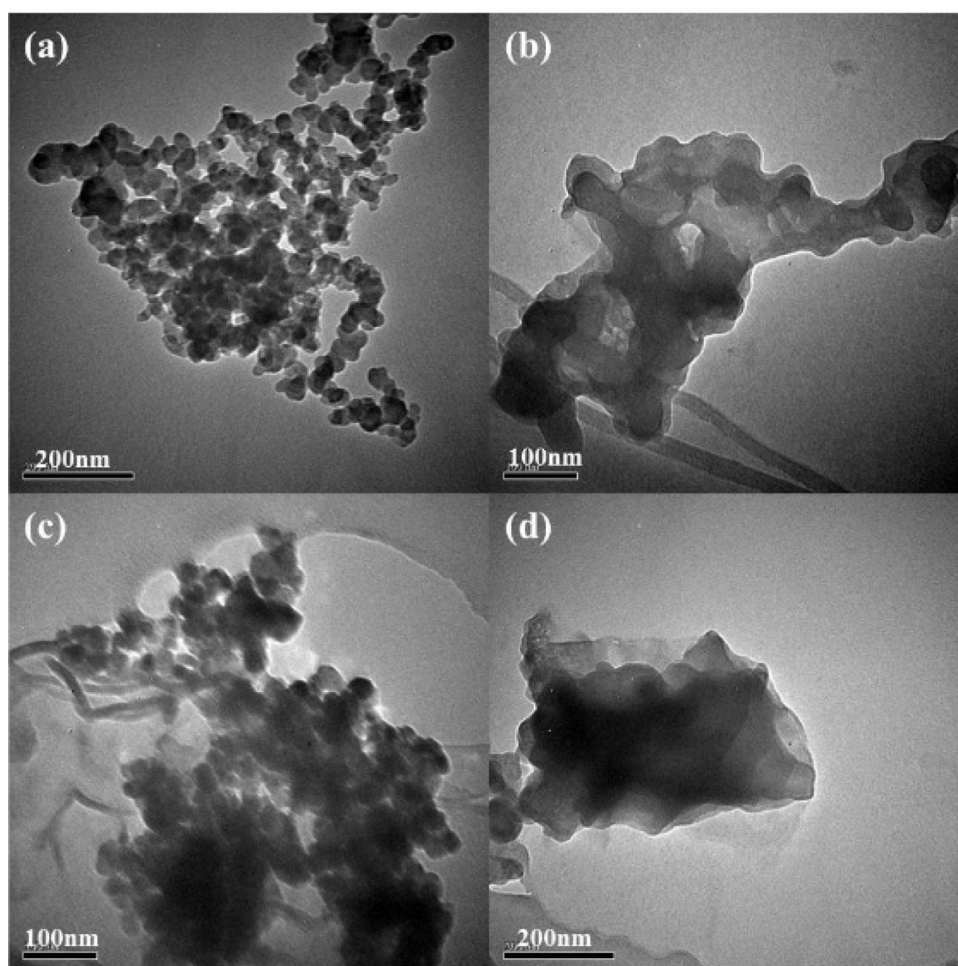


Fig. 5. TEM images of (a) M0, (b) M400, (c) M0 + g-C₃N₄ and (d) g-C₃N₄.

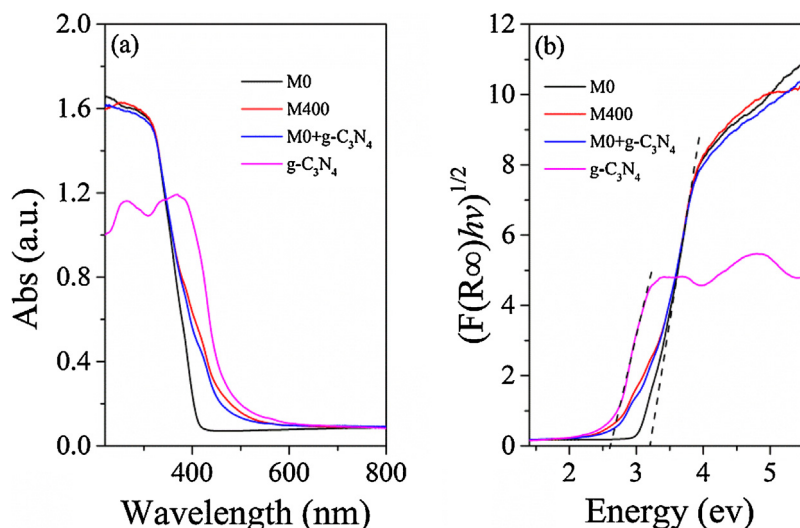


Fig. 6. (a) UV-vis diffuse reflectance spectra and (b) plots of transformed Kubelka–Munk function versus the energy of absorbed light for the M0, M400, M0 + g-C₃N₄ and g-C₃N₄.

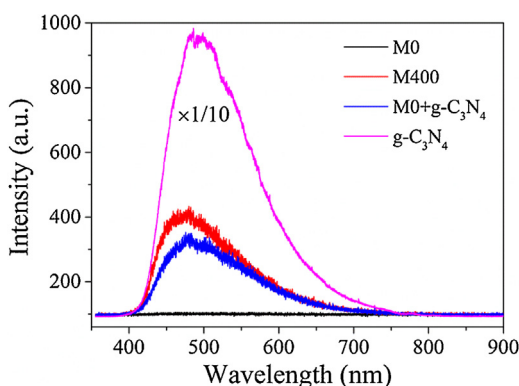


Fig. 7. The photoluminescence (PL) emission spectra of the M0, M400, M0 + g-C₃N₄ and g-C₃N₄.

sized photocatalysts were calculated by plots of $(F(R_{\infty})/h\nu)^{1/2}$ versus photo energy, as shown in Fig. 6b. The absorption onset of g-C₃N₄ is at about 475 nm, corresponding to a band gap energy of 2.6 eV. This is consistent with previous work [12]. The band gap of M0 is about 3.2 eV, with an absorption edge of 384 nm. After hybridization with g-C₃N₄, the absorbance of M400 and M0 + g-C₃N₄ is extended to the visible region due to the presence of g-C₃N₄. Compared to M0, no significant shift of the absorption edge occurs, indicating similar band gap energies. This composite photocatalyst can improve the utilization of the visible light.

3.5. Photoluminescence emission spectra

PL emission spectra of the photocatalysts are shown in Fig. 7, revealing that the peaks are nearly identical in shape and position for all of the photocatalysts. The PL intensity of M400 and M0 + g-C₃N₄ was significantly reduced in comparison with pure g-C₃N₄, indicating that the electron-hole recombination on the surface of these photocatalysts was largely inhibited, to generate more photoelectrons and holes to participate in the photocatalytic reaction. This may be because the heterojunction formed at the interface between g-C₃N₄ and P25 can prevent the recombination of photo-generated charge effectively. The PL intensity of M0 is

low, probably because the amount of photogenerated electron-hole pairs is lower under the same irradiation conditions. Similar results were observed on the red phosphorus/g-C₃N₄ and BiOBr/g-C₃N₄ heterojunction systems by other groups [15,45].

3.6. Electron paramagnetic resonance spectra

To understand the performance difference between M400 and M0 + g-C₃N₄, DMPO spin-trapping EPR measurements were employed in methanol dispersion for DMPO-•O₂⁻ and aqueous dispersion for DMPO-•OH. The characteristic peaks of both •O₂⁻ and •OH radicals can be observed under visible light and UV light illumination (Fig. 8). The signal of •O₂⁻ is much stronger than that of •OH under visible light. This is because visible light can only excite g-C₃N₄, and the valence band (VB) holes (~1.40 eV) from g-C₃N₄ cannot directly oxidize OH⁻ or H₂O into •OH radicals (1.99 eV for OH⁻/•OH and 2.37 eV for H₂O/•OH). The •OH radicals should be generated via the •O₂⁻ → H₂O₂ → •OH route. These results confirm that •O₂⁻ is the main active species, and •OH plays a minor role in NO_x oxidation under visible light. In addition, the VB holes of g-C₃N₄ might also oxidize NO because the $E_{\phi VB}$ (~1.4 eV versus normal hydrogen electrode (NHE)) of g-C₃N₄ is more positive than $E_{\phi}(\text{NO}_2/\text{NO}, 1.03 \text{ eV versus NHE})$, $E_{\phi}(\text{HNO}_2/\text{NO}, 0.99 \text{ eV versus NHE})$, and $E_{\phi}(\text{HNO}_3/\text{NO}, 0.94 \text{ eV vs NHE})$ [10]. As shown in Fig. 1, the conversion of NO was similar over M400 and M0 + g-C₃N₄; however, the NO₂ selectivity over M400 was lower than that over M0 + g-C₃N₄, and therefore the NO_x conversion was higher over M400. These results indicated that •O₂⁻ is the main active species for the NO oxidation to NO₃⁻ under visible light.

The signal of •O₂⁻ is similar to that of •OH under UV light. This is because UV light can excite both TiO₂ and g-C₃N₄. The VB holes (~2.85 eV) from TiO₂ can directly oxidize OH⁻ or H₂O into •OH radicals (1.99 eV for OH⁻/•OH and 2.37 eV for H₂O/•OH), and the conduction bands (CB) from both TiO₂ (~-0.35 eV) and g-C₃N₄ (~-1.39 eV) can directly reduce the O₂ to •O₂⁻ radicals (-0.33 eV for O₂/•O₂⁻). These results confirm that •O₂⁻, •OH and VB holes play a role in NO_x oxidation under UV light. As shown in Fig. 8, the signal of •O₂⁻ is higher than that of •OH over M400, and the signal of •O₂⁻ is lower than that of •OH over M0 + g-C₃N₄. Combined with the activity data in Fig. 2, this indicated that •O₂⁻ is the main active species for the NO oxidation to NO₃⁻ under UV light.

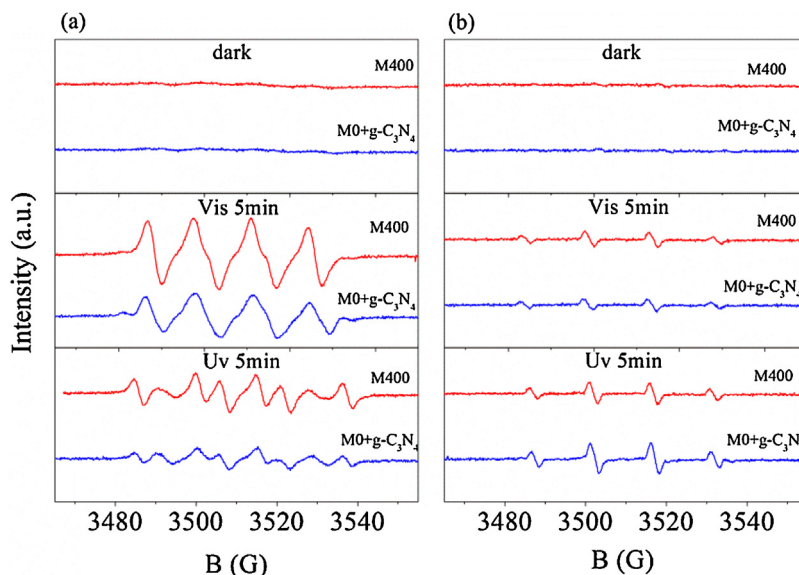


Fig. 8. DMPO spin-trapping EPR spectra of M400 and M0 + g-C₃N₄ (a) methanol dispersion for DMPO·O₂⁻ and (b) aqueous dispersion for DMPO·OH.

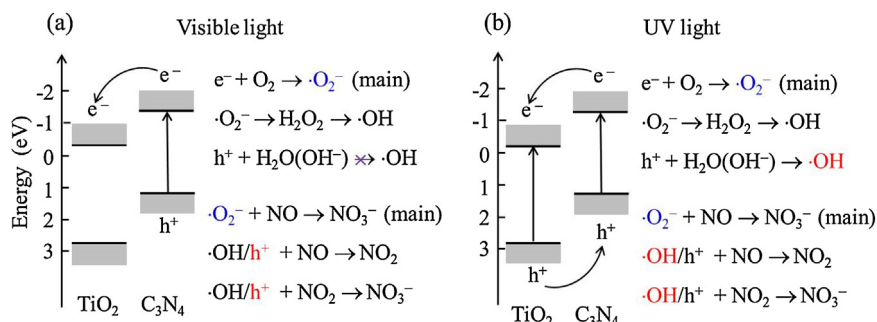


Fig. 9. Schematic illustration of the charge transfer, radical generation and NO oxidation on g-C₃N₄-TiO₂ under visible and UV light irradiation.

On the basis of the above results and discussion, the photocatalytic mechanism for the M400 and M0 + g-C₃N₄ is tentatively proposed and schematically illustrated in Fig. 9. Under visible light irradiation, g-C₃N₄ can be excited to induce the formation of photo-generated electrons and holes. The electrons could then migrate from the CB of g-C₃N₄ to the CB of TiO₂ via their interfacial interaction (Fig. 9a). Because interfacial interaction of M400 is better than that of M0 + g-C₃N₄, more electrons in g-C₃N₄ (CB) could easily transfer to TiO₂ (CB) in M400, and then more $\cdot O_2^-$ radical is generated, which is responsible for the NO oxidation to NO₃⁻ under visible light. Under UV light irradiation, both TiO₂ and g-C₃N₄ can be excited to induce the formation of photo-generated electrons and holes (Fig. 9b). The electrons in g-C₃N₄ (CB) could easily transfer to TiO₂ (CB), and the holes in TiO₂ (VB) could also easily transfer to g-C₃N₄ (VB) through their interfacial interaction. As a result, the recombination of the photo-generated electrons and holes is suppressed [46]. Because the interfacial interaction of M400 is better than that of M0 + g-C₃N₄, more electrons and holes were transferred; the holes transferred to g-C₃N₄ cannot directly oxidize OH⁻ or H₂O into $\cdot OH$ radicals, leading to more $\cdot O_2^-$ radical and less $\cdot OH$ on M400 (Fig. 8).

4. Conclusions

In summary, g-C₃N₄-TiO₂ composite photocatalysts were successfully prepared via a simple one-step calcination method utilizing commercial P25 and melamine as the precursors. Characterization results confirmed the formation of g-C₃N₄-TiO₂ composite photocatalysts, in which the TiO₂ nanoparticles are embedded in the g-C₃N₄ lamellar structure. The introduced g-C₃N₄ shows a great influence on the photocatalytic activity of the TiO₂. At the optimal g-C₃N₄ content (~15 wt%), the conversion of NO_x was enhanced under visible light and UV light. The conversion of NO_x on M0 + g-C₃N₄, which was prepared by the mechanical mixing of g-C₃N₄ and TiO₂ (the content of g-C₃N₄ is the same as for M400), was lower than that on M400. Therefore, the interaction of g-C₃N₄ and P25 is critical for the activity. Raman, TEM and XPS results indicate that g-C₃N₄ is more uniformly dispersed on the surface of M400 than on M0 + g-C₃N₄. The electron-hole recombination on the surface of M400 and M0 + g-C₃N₄ was significantly reduced in comparison with pure g-C₃N₄. EPR results indicated that $\cdot O_2^-$ is the main active species for the NO oxidation to NO₃⁻ under visible and UV light. Because the interfacial interaction of M400 is better than that of M0 + g-C₃N₄, more electrons in g-C₃N₄ (CB) could easily transfer to TiO₂ (CB) in M400, so that more $\cdot O_2^-$ radical is generated under visible light; on the other hand, more electrons

and holes were transferred under UV light, and the hole transfer to g-C₃N₄ cannot directly oxidize OH[−] or H₂O into •OH radicals, leading to more •O₂[−] radical and less •OH on M400. These phenomena are responsible for the difference in activity between M400 and M0+g-C₃N₄ for the oxidation of NO to NO₃[−]. The present study can improve our understanding of NO removal on the photocatalyst surface and the mechanism for the enhancement of activity by the formation of g-C₃N₄-TiO₂.

Acknowledgments

This work was supported by the National Natural Science Foundation of China, (21207145) and the Strategic Priority Research Program of the Chinese Academy of Sciences, (XDB05050600). This work was also supported by the National Natural Science Foundation of China, (51221892).

Appendix A. Supplementary data

Supplementary data associated with this article can be found, in the online version, at <http://dx.doi.org/10.1016/j.apcatb.2015.11.013>.

References

- [1] B. Zhao, S.X. Wang, H. Liu, J.Y. Xu, K. Fu, Z. Klimont, J.M. Hao, K.B. He, J. Cofala, M. Amann, *Atmos. Chem. Phys.* 13 (2013) 9869–9897.
- [2] H. He, Y.S. Wang, Q.X. Ma, J.Z. Ma, B.W. Chu, D.S. Ji, G.Q. Tang, C. Liu, H.X. Zhang, J.M. Hao, *Sci. Rep.* 4 (2014) 4172, DOI:10.1038/srep04172.
- [3] Z.H. Ai, W.K. Ho, S.C. Lee, *J. Phys. Chem. C* 115 (2011) 25330–25337.
- [4] F. Dong, Y.J. Sun, M. Fu, W.-K. Ho, S.C. Lee, Z.B. Wu, *Langmuir* 28 (2012) 766–773.
- [5] H. Yamashita, K. Yoshizawa, M. Ariyuki, S. Higashimoto, M. Che, M. Anpo, *Chem. Commun.* (2001) 435–436.
- [6] J.L. Zhang, T. Ayusawa, M. Minagawa, K. Kinugawa, H. Yamashita, M. Matsuoka, M. Anpo, *J. Catal.* 198 (2001) 1–8.
- [7] J.L. Zhang, Y. Hu, M. Matsuoka, H. Yamashita, M. Minagawa, H. Hidaka, M. Anpo, *J. Phys. Chem. B* 105 (2001) 8395–8398.
- [8] F. Dong, Y. Huang, S.C. Zou, J.A. Liu, S.C. Lee, *J. Phys. Chem. C* 115 (2011) 241–247.
- [9] G.H. Dong, W.K. Ho, L.Z. Zhang, *Appl. Catal. B* 168–169 (2015) 490–496.
- [10] F. Dong, Z.Y. Wang, Y.H. Li, W.-K. Ho, S.C. Lee, *Environ. Sci. Technol.* 48 (2014) 10345–10353.
- [11] F. Dong, Q.Y. Li, Y.J. Sun, W.-K. Ho, *ACS Catal.* 4 (2014) 4341–4350.
- [12] X.C. Wang, S. Blechert, M. Antonietti, *ACS Catal.* 2 (2012) 1596–1606.
- [13] Y.H. Zhang, Q.W. Pan, G.Q. Chai, M.R. Liang, G.P. Dong, Q.Y. Zhang, J.R. Qiu, *Sci. Rep.* 3 (2013) 1943, <http://dx.doi.org/10.1038/srep01943>.
- [14] J. Liu, Y. Liu, N.Y. Liu, Y.Z. Han, X. Zhang, H. Huang, Y. Lifshitz, S.-T. Lee, J. Zhong, Z.H. Kang, *Science* 347 (2015) 970–974.
- [15] Y.J. Sun, W.D. Zhang, T. Xiong, Z.W. Zhao, F. Dong, R.Q. Wang, W.-K. Ho, *J. Colloid Interface Sci.* 418 (2014) 317–323.
- [16] T. Sano, S. Tsutsui, K. Koike, T. Hirakawa, Y. Teramoto, N. Negishi, K. Takeuchi, *J. Mater. Chem. A* 1 (2013) 6489–6496.
- [17] F. Dong, Z.W. Zhao, T. Xiong, Z.L. Ni, W.D. Zhang, Y.J. Sun, W.-K. Ho, *ACS Appl. Mater. Interfaces* 5 (2013) 11392–11401.
- [18] J.S. Zhang, J.H. Sun, K. Maeda, K. Domen, P. Liu, M. Antonietti, X.Z. Fu, X.C. Wang, *Energy Environ. Sci.* 4 (2011) 675–678.
- [19] F. Goettmann, A. Fischer, M. Antonietti, A. Thomas, *Angew. Chem. Int. Ed.* 45 (2006) 4467–4471.
- [20] M. Groenewolt, M. Antonietti, *Adv. Mater.* 17 (2005) 1789–1792.
- [21] S.C. Lee, H.O. Lintang, L. Yuliati, *Chem. -Asian J.* 7 (2012) 2139–2144.
- [22] X.C. Wang, K. Maeda, X.F. Chen, K. Takanebe, K. Domen, Y.D. Hou, X.Z. Fu, M. Antonietti, *J. Am. Chem. Soc.* 131 (2009) 1680–1681.
- [23] K. Dai, L.H. Lu, C.H. Liang, Q. Liu, G.P. Zhu, *Appl. Catal. B* 156 (2014) 331–340.
- [24] J.Y. Lei, Y. Chen, L.Z. Wang, Y.D. Liu, J.L. Zhang, *J. Mater. Sci.* 50 (2015) 3467–3476.
- [25] X.F. Lu, Q.L. Wang, D.L. Cui, *J. Mater. Sci. Technol.* 26 (2010) 925–930.
- [26] K. Sridharan, E. Jang, T.J. Park, *Appl. Catal. B* 142 (2013) 718–728.
- [27] Z.A. Huang, Q. Sun, K.L. Lv, Z.H. Zhang, M. Li, B. Li, *Appl. Catal. B* 164 (2015) 420–427.
- [28] X.-X. Zou, G.-D. Li, Y.-N. Wang, J. Zhao, C. Yan, M.-Y. Guo, L. Li, J.-S. Chen, *Chem. Commun.* 47 (2011) 1066–1068.
- [29] J.W. Zhou, M. Zhang, Y.F. Zhu, *Phys. Chem. Chem. Phys.* 17 (2015) 3647–3652.
- [30] L.A. Gu, J.Y. Wang, Z.J. Zou, X.J. Han, *J. Hazard. Mater.* 268 (2014) 216–223.
- [31] X.S. Zhou, F. Peng, H.J. Wang, H. Yu, Y.P. Fang, *Chem. Commun.* 47 (2011) 10323–10325.
- [32] M. Fu, J.M. Pi, F. Dong, Q.Y. Duan, H. Guo, *Int. J. Photoenergy* (2013) 158496.
- [33] J.C. Shen, H. Yang, Q.H. Shen, Y. Feng, Q.F. Cai, *CrystEngComm* 16 (2014) 1868–1872.
- [34] M.J. Munoz-Batista, A. Kubacka, M. Fernandez-Garcia, *Catal. Sci. Technol.* 4 (2014) 2006–2015.
- [35] G.Y. Li, X. Nie, Y.P. Gao, T.C. An, *Appl. Catal. B* 180 (2016) 726–732.
- [36] H.Q. Wang, J.Z. Li, C.C. Ma, Q.F. Guan, Z.Y. Lu, P.W. Huo, Y.S. Yan, *Appl. Surf. Sci.* 329 (2015) 17–22.
- [37] J.G. Yu, S. Wang, J.X. Low, W. Xiao, *Phys. Chem. Chem. Phys.* 15 (2013) 16883–16890.
- [38] H.L. Zhu, D.M. Chen, D. Yue, Z.H. Wang, H. Ding, *J. Nanopart. Res.* 16 (2014) 1–10.
- [39] J.Z. Ma, H.M. Wu, Y.C. Liu, H. He, *J. Phys. Chem. C* 118 (2014) 7434–7441.
- [40] J.Z. Ma, H. He, F.D. Liu, *Appl. Catal. B* 179 (2015) 21–28.
- [41] F. Dong, Y.J. Sun, L.W. Wu, M. Fu, Z.B. Wu, *Catal. Sci. Technol.* 2 (2012) 1332–1335.
- [42] J. Zhang, M.J. Li, Z.C. Feng, J. Chen, C. Li, *J. Phys. Chem. B* 110 (2006) 927–935.
- [43] Q.J. Xiang, J.G. Yu, M. Jaroniec, *J. Phys. Chem. C* 115 (2011) 7355–7363.
- [44] J.Z. Jiang, O.Y. Lei, L.H. Zhu, A.M. Zheng, J. Zou, X.F. Yi, H.Q. Tang, *Carbon* 80 (2014) 213–221.
- [45] Y.-P. Yuan, S.-W. Cao, Y.-S. Liao, L.-S. Yin, C. Xue, *Appl. Catal. B* 140 (2013) 164–168.
- [46] G.Y. Li, X. Nie, J.Y. Chen, Q. Jiang, T.C. An, P.K. Wong, H.M. Zhang, H.J. Zhao, H. Yamashita, *Water Res.* (2016), <http://dx.doi.org/10.1016/j.watres.2015.1005.1053> (in press).